applied sciences

MDPI

Article

Masked Stereolithography of a Metacarpal Fixation Plate Prototype with a Low-Temperature Barium Titanate Coating

Eduard G. Tuns [1], Razvan Păcurar [1] and Mircea Năsui [2,3,*]

[1] Department of Manufacturing Engineering, Faculty of Industrial Engineering, Robotics and Production Management, Technical University of Cluj-Napoca, Blv. Muncii, No. 103-105, 400641 Cluj-Napoca, Romania; eduardgtuns@icloud.com (E.G.T.); razvan.pacurar@tcm.utcluj.ro (R.P.)
[2] Centre for Superconductivity, Spintronics and Surface Science, Physics and Chemistry Department, Technical University of Cluj-Napoca, Str. Memorandumului No. 28, 400028 Cluj-Napoca, Romania
[3] Institute of Nanomaterials and Nanotechnologies—Eutinn, European University of Technology, European Union, 400114 Cluj-Napoca, Romania
* Correspondence: mircea.nasui@chem.utcluj.ro

Featured Application

Early-stage low-profile, $BaTiO_3$-coated fixation plate prototype fabricated by accessible masked stereolithography, for further mechanical and biological evaluation.

Abstract

Fifth metacarpal shaft fractures account for a large share of hand trauma and often require operative internal fixation, yet conventional dorsal plates and cannulated screws present a stiffness mismatch with native bone and the insertion of screws can shear surface coatings. This study presents the design, fabrication, and preliminary characterisation of a low-profile, $BaTiO_3$-coated dorsal fixation plate prototype for the fifth metacarpal bone. A curved, 0.5 mm plate was modelled in SolidWorks and overlaid with a randomised Delaunay lattice in Meshmixer, achieving 73.6% porosity with a 70% mesh reduction strategy. A linear static finite element study of a simplified periodic surrogate of the plate (nominal polymer properties, 300 N load) is reported only as an illustrative response, not as evidence of mechanical suitability. Plates were manufactured by masked stereolithography in a water-washable resin not intended for implantation (not MED610), with an average accuracy of 98.77% on three features measured before coating; the dimensions after the 120 °C and 180 °C coating steps were not remeasured. A barium titanate precursor was synthesised via the propionate route and deposited through a three-cycle, low-temperature (120 °C) submersion process followed by a solvothermal treatment at 180 °C for 1 h. Optical microscopy and SEM/EDS showed qualitative surface coverage with barium and titanium and open pores, and XRD showed reflections consistent with perovskite $BaTiO_3$; the polymorph, thickness, adhesion, uniformity and mechanical stability of the coating were not quantified. Under cyclic compressive loading (1–2 N), a coated plate dried at 120 °C, before the solvothermal step was introduced, generated an alternating open-circuit voltage of 0.62 ± 0.08 V at 1 N and 0.93 ± 0.10 V at 2 N (peak-to-peak), much larger than that of an uncoated plate; its origin remains to be established. This is a fabrication and preliminary characterisation study of a non-biocompatible prototype: mechanical testing of the printed structure, poled and replicate electrical measurements, and biological evaluation have not yet been performed and are the next steps.

Keywords: metacarpal fixation plate; 3D printing; masked stereolithography; Delaunay lattice; barium titanate; barium titanate coating; proof-of-concept prototype

Check for updates

Academic Editors: José Luis Rivera-Armenta and Cynthia G. Flores-Hernández

Received: 9 September 2026
Revised: 11 October 2026
Accepted: 16 October 2026
Published: 19 October 2026

Copyright: © 2026 by the authors. Licensee MDPI, Basel, Switzerland. This article is an open access article distributed under the terms and conditions of the Creative Commons Attribution (CC BY) license.

1. Introduction

Hand injuries represent one of the most frequent reasons for emergency room admissions worldwide, commonly resulting from direct trauma or falls onto an outstretched hand. Within hand anatomy, metacarpal fractures are the most prevalent, comprising between 18% and 44% of all hand-related skeletal injuries [1]. Among the five metacarpal bones, clinical data reveal that the fifth and smallest metacarpal bone is particularly fragile and statistically the most prone to fracture localisation across all patient age groups, accounting for 49% of all metacarpal fractures in patients under 16 years of age and escalating to 58% in adults over 16 [2]. While fractures located at the neck or base of the metacarpal are frequently managed using non-operative methods, fractures sustained along the bone shaft require operative internal fixation in 43.2% of cases [1]. This emphasises that injuries along the length of the fifth metacarpal bone shaft present a clear clinical requirement for specialised surgical remediation hardware.

Historically, open reduction and internal fixation (ORIF) of metacarpal shaft fractures has relied on surface-mounted dorsal plates for skeletal alignment, such as the Stryker Profyle 3D line [3]. Although effective at suppressing fracture non-unions and preventing excessive malunions, conventional plate profiles require extensive disruption of the enveloping soft tissue and aggressive periosteal stripping during surgical exposure, which severely impairs local vascularity and delays cortical bone regeneration [4]. Furthermore, standard metallic plates create a massive mechanical mismatch between the plate and the native bone (10–30 GPa), inducing the stress shielding effect that causes the underlying bone to atrophy and resorb due to lack of physiological loading, as that is taken over entirely by the implant [5]. Additionally, the prominent physical profile of legacy hardware generates chronic extensor tendon friction during normal finger movement, which may lead to painful tissue adhesions or tendon rupture [4].

Vat photopolymerisation and lattice design. Bukhari et al. [6] reviewed vat photopolymerisation of smart polymers for biomedical applications, and the Stratasys design guide [7] gives design rules for fine printed features, including the removal of support and uncured material from internal channels. Zenobi et al. [8] tailored the microarchitecture of printed bone-like scaffolds, and Kanwar et al. [9] proposed a method to design printable stochastic scaffolds with controlled porosity for bone tissue engineering. For the mechanics of such structures, Mueller et al. [10] compared the energy absorption of periodic and stochastic lattices, and Yamada et al. [11] designed a strut-based stochastic lattice from the structural and mechanical characteristics of cancellous bone. These works treat the lattice as a passive mechanical or tissue engineering structure; none of them adds an electroactive surface to a thin fixation plate.

Piezoelectricity of bone and piezoelectric biomaterials. Zhou et al. [12] described the molecular mechanism of polarisation in collagen, which underlies the piezoelectricity of bone. Jacob et al. [13], Ganeson et al. [14] and Zhang et al. [15] reviewed piezoelectric biomaterials, devices and systems for bone, cartilage and orthopaedic applications, and Carter et al. [16] discussed the converse piezoelectric effect as a way to apply mechanical stimulation for bone regeneration. Zheng et al. [17] reported that the nanostructure of tetragonal $BaTiO_3$ coatings, through their piezoelectric effect, influenced the shape and osteogenic differentiation of bone mesenchymal stem cells. None of these works deposits the piezoelectric phase on a printed photopolymer part.

Barium titanate processing and porous scaffolds. Sahoo et al. [18] reviewed the design of porous scaffolds for tissue engineering and regenerative medicine, and Shyeed et al. [19] reviewed polymer-based smart materials for 4D printing. Our previous work [20] obtained oriented, piezoelectric $BaTiO_3$ thin films from the propionate-route solution used here, but on NiW metallic substrates and after annealing at 700–800 °C in Ar–H2. Such temperatures

exceed what a photopolymer scaffold can withstand, so a lower-temperature route is needed for printed polymer parts.

Fixation hardware as a coating carrier. The AO surgical reference [21] describes the insertion of headless compression screws, in which the thread is driven into bone under torque, and Murawski et al. [22] reported thread delamination of 4.5 mm AO cannulated screws in paediatric trauma patients. Moura Neto et al. [23] analysed the microstructure and thermal behaviour of castor polyurethane osteosynthesis plates, an example of polymer plates considered for fracture fixation. A coating carried on a screw thread is therefore exposed to insertion shear, whereas a plate seated on the bone surface is not, which is why a plate is used as the carrier here.

Validation of printed fixation parts. Salerno et al. [24] proposed a methodology for the dimensional and mechanical analysis of printed surgical guides, including the change in scan-to-CAD deviation after sterilisation, and Tilton et al. [25] combined finite element modelling with biomechanical testing of the same additively manufactured fracture fixation implants. In the present study, only the first part of such a validation, a dimensional check, is carried out on the printed plate (Section 3.4).

Functioning instead as an additional surface-level architecture positioned along the tension side of the metacarpal, the proposed plate is intended to avoid insertion shear on the coating; whether it can convert post-operative bending into a useful electrical stimulus, and whether this would aid bone regeneration, remains to be tested [16]. Building on this rationale, the present study designs, manufactures and preliminarily characterises a $BaTiO_3$-coated dorsal fixation plate prototype for the fifth metacarpal bone. The prototype combines a randomised, reduction-decimated Delaunay lattice—intended to favour a bending-dominated response rather than the layer collapse failure typical of periodic unit cells—with a barium titanate coating applied through a low-temperature cyclic submersion process followed by a solvothermal step, with FTIR used to look for interaction between the coating and the resin. The two central contributions of this work are therefore (i) the constructive technological design of the CAD/lattice plate geometry with an illustrative finite element study on a periodic surrogate, and (ii) the synthesis, deposition and structural characterisation of a $BaTiO_3$ coating on the printed scaffold, together with a first electrical test.

We are not aware of earlier work that combines, within a single workflow on a consumer-grade printer, three elements that have so far been addressed separately: (i) a low-profile (0.5 mm), anatomically curved dorsal plate positioned on the tension side of the fifth metacarpal, which is intended to reduce soft-tissue disruption and avoid the insertion torque of cannulated screws; (ii) a randomised, 70%-reduced Delaunay lattice that replaces periodic unit cells, intended to shift the failure mode from layer collapse to a bending-dominated response (not yet verified on printed parts), with 73.6% porosity; and (iii) a low-temperature (120 °C drying, 180 °C solvothermal), three-cycle propionate-route $BaTiO_3$ coating that preserved the open pores of the polymer scaffold. Methodologically, the entire chain—design, printing (20 µm layers; 98.77% average accuracy on three features, measured before coating), post-processing and coating—is carried out on a consumer-grade masked stereolithography printer without high-temperature ceramic processing. Practically, the coated plate gave a peak-to-peak open-circuit voltage of 0.62 ± 0.08 V at 1 N and 0.93 ± 0.10 V at 2 N under cyclic loading, much larger than that of an uncoated plate; its origin is not yet established. This is an early-stage prototype study: the printing resin is not biocompatible, the lattice has not been mechanically tested, and no biological evaluation was performed.

Three gaps motivate this work. First, vat-photopolymerised lattice plates and scaffolds [6–9] have mostly been studied as mechanical or tissue engineering structures without

an electroactive surface. Second, piezoelectric $BaTiO_3$ coatings [17–20] are usually deposited on metallic or ceramic substrates or processed at temperatures that polymer parts cannot withstand. Third, low-profile plates that avoid screw insertion torque [15,21–23] have not, to our knowledge, been combined with such coatings. The present study addresses these gaps at prototype level only.

2. Materials and Methods

2.1. Design of the CAD Metacarpal Plate

The base shape was created as a C-shaped cross-section extruded into a cylindrical sector mirroring the natural dorsal curvature of the fifth metacarpal, with sharp edges rounded to an R0.2 mm fillet to eliminate stress concentrators and smooth the tissue contact surface. Sizing parameters were derived from clinical averages: an internal radius of 5 mm and an overall length compatible with the average 52.3 mm length of the Metacarpal-5 bone [2]. The plate has an overall length of 50 mm and a cross-sectional arc sweep angle of 135°. A minimal thickness of 0.5 mm was selected so that the plate sits functionally flush beneath the soft tissue, mitigating extensor tendon friction; this thin-wall precision is achievable owing to the high resolution of the MSLA printing process described in Section 2.2. The model was then partitioned into a central active zone, which would host the porous lattice scaffold, and two lateral technological zones intended for fastening hardware (Figure 1).

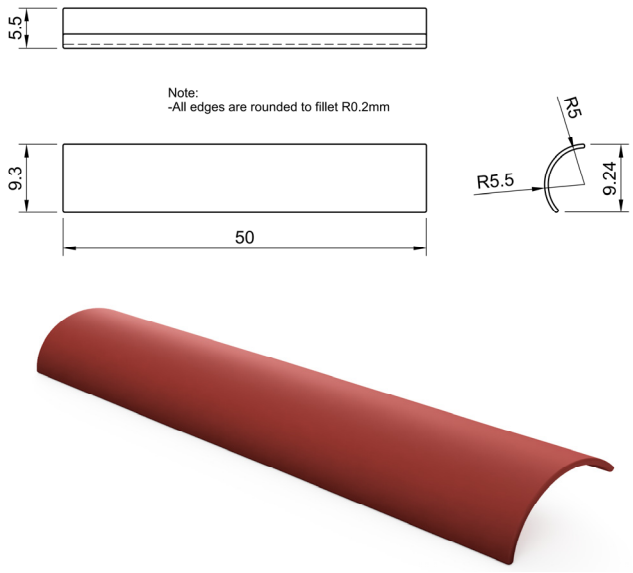


Figure 1. (**Bottom**) A render of the primordial CAD model of the metacarpal plate; (**Top**) technical drawing.

Conventional periodic lattices, such as cubic unit cells, are highly anisotropic: loaded parallel to their struts ($\alpha = 0°$), they behave rigidly in a stretch-dominated mode, but a 15–30° change in load angle triggers strut bending and a sharp drop in yield strength [10], a serious limitation for hand hardware, which is routinely subjected to shear and off-axis loading (Figure 2). The Delaunay mesh instead behaves as a redundant, body-centred-cubic-like grid with struts oriented along both $\alpha = 0°$ and $\alpha = 45°$, keeping most struts in tension or compression rather than bending across the loading range and giving a stretch-dominated response at any orientation [10]. Left unmodified, a fully periodic Delaunay mesh can still fail through sequential horizontal layer collapse, visible as cyclical stress dips once one load-bearing layer fails before the layer beneath begins carrying load [10]. This

was addressed by manipulating the "Reduce" parameter in Meshmixer from 100% to 70%, deliberately breaking the aligned planes of the periodic triangulation.

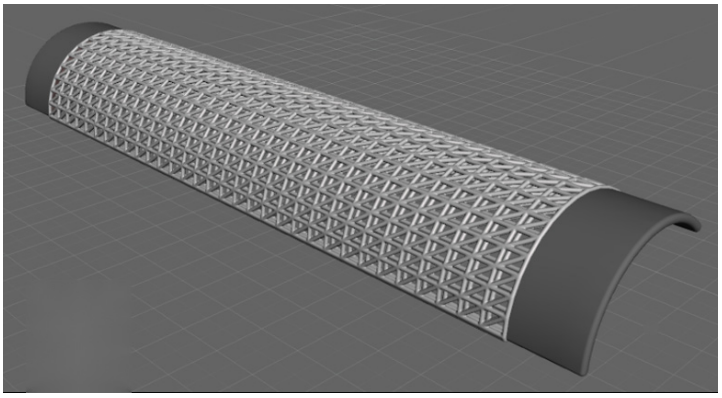


Figure 2. The finalised mesh model, generated with the "Make Pattern" function of Meshmixer (Mesh + Delaunay pattern, 0.25 mm element dimension, mesh reduction set to 70%).

This decimation is expected to change the failure mode from sequential layer collapse to a more progressive response and to bring the scaffold closer to quasi-isotropic behaviour at the macroscopic scale, with a more uniform load distribution under multi-axial loading [10,11]. This expectation is inferred from the literature and from the geometry; it has not been verified on the printed plate (Section 3.4). The resulting porosity of the active zone, calculated from the CAD model as $1 - V_{lattice}/V_{solid}$, is 73.6% (72.6% for the periodic surrogate used in the FEA); it follows directly from replacing the solid 0.5 mm wall with 0.25 mm struts, and the 70% reduction increases it further by removing edges and vertices of the triangulation.

2.2. Printing and Post-Processing

The plates were printed on an Anycubic Photon Mono 2K masked stereolithography (MSLA) printer in Anycubic Water Washable Resin+ (Anycubic, Shenzhen, China), with a layer height of 20 µm, an exposure time of 2–2.8 s per layer and automatically generated supports. This resin is not intended for implantation and was used only to manufacture the prototype; it is not MED610, whose nominal properties were used in the finite element study (Section 2.4). After printing, the parts were washed by agitated water immersion and cleared of residual resin with compressed air, and post-cured in a UV chamber for about 5 min on a rotating base.

2.3. Barium Titanate (BTO) Coating

To prepare the $BaTiO_3$ (BTO) coating solution, barium propionate and titanium (IV) isopropoxide were combined in a stoichiometric, equimolar ratio. The barium propionate solution was first synthesised through the propionate route at room temperature, using a mixture of barium acetate, methanol (CH_3OH), propionic acid (CH_3CH_2COOH) and ammonia (NH_4OH); propionic acid was chosen for its low boiling point (140 °C), which simplifies processing. The barium propionate solution was then mixed with a titanium (IV) isopropoxide solution (boiling point 232 °C), and the total concentration of the combined precursor mixture was adjusted to 0.2 M [20]. The precursor solution was applied to the printed scaffolds by a cyclic submersion procedure, alternating liquid immersion with thermal drying and ambient relaxation. In each cycle, the scaffold was submerged in the BTO solution for 3 min so that the liquid could penetrate the Delaunay lattice and wet the struts. After removal and drainage of the excess liquid, the sample was placed on a ceramic plate and dried in an oven at 120 °C for 25 min in the first cycle, and for a shorter

15 min in the second and third cycles, which were intended to improve the homogeneity of the preceding layer. To promote crystallisation of the deposited layer, the coated scaffold was then subjected to a solvothermal (hydrothermal-type) treatment at 180 °C for 1 h. The scaffold was immersed in a reaction medium containing barium acetate, methanol, ammonia and titanium (IV) isopropoxide and heated in a sealed Teflon-lined autoclave. The solvothermal step was introduced after the first submission. The scaffolds examined by FTIR and optical microscopy (Section 3.2) and the plate used for the voltage test (Section 3.3) were therefore processed only up to the 120 °C drying cycles, whereas the XRD pattern and the SEM/EDS maps (Section 3.2) were recorded after the solvothermal treatment. The drying temperature of 120 °C was selected to evaporate the volatile organic components; dimensional stability of the scaffold after the 120 °C and 180 °C steps was not checked (Section 3.4).

2.4. Finite Element Model

A linear static finite element analysis was run in SolidWorks (SP4.1 2026) Simulation on a periodic perforated surrogate of the active zone (porosity 72.6%). The printed Delaunay lattice could not be analysed directly: the generated mesh comprised approximately 790,000 triangular facets, whereas SolidWorks converts .stl files into solid bodies only up to 20,000 facets, and decimating the lattice to that limit destroyed the strut topology. The material was assigned the nominal properties of MED610 ($E = 2500$ MPa, $\nu = 0.35$, tensile strength 55 MPa), not those of the printed resin, which were not measured. The technological zones were fixed and a normal force of 300 N, representative of the fracture load of the intact bone [3], was applied as a uniform normal load over the entire outer (dorsal) face of the plate, including the technological zones (approximately 478 mm^2 after subtraction of the holes, corresponding to a nominal pressure of about 0.63 MPa). Because the face is curved (135° arc), the load acts normal to the surface at each point, and its resultant in the dorsal–palmar direction is lower than 300 N. The surrogate was meshed with the default SolidWorks mesher at the default density setting, using tetrahedral solid elements; the specific element size and count were not recorded. A mesh convergence study was not performed. The span was left unsupported, so the model represents a plate bridging a fracture gap and carrying the whole load; this is a limiting case and not a model of physiological loading. The study is limited to small-displacement linear behaviour; buckling and large-displacement effects were not analysed, and the von Mises stress was not extracted.

2.5. Characterisation Techniques

Dimensional fidelity of the printed scaffold was assessed with a high-resolution Optika optical microscope, comparing three nominal CAD dimensions, the technological zone width (A) and the length (B) and height (C), of a Delaunay unit cell against the corresponding measurements on the printed part, the latter two averaged across multiple cells to exclude outliers. Accuracy per variable was calculated as one minus the relative deviation between the nominal and measured value, expressed as a percentage. Post-coating surface characterisation used the same optical microscope to compare a BTO-coated sample against an uncoated control, examining surface sheen, transparency, and cross-sectional strut and pore integrity. Possible interaction between the coating and the resin was examined by FTIR, comparing a BTO-submerged scaffold with an unsubmerged one. The crystalline phase of the coating was examined by grazing-incidence X-ray diffraction (GIXRD) on the coated plate (Bruker D8 DISCOVER, Karlsruhe, Germany), and the surface morphology and elemental distribution by scanning electron microscopy with energy-dispersive spectroscopy using a Crossbeam System Neon 40ESB from Carl Zeiss (Jena,

Germany). The electrical response of the coated plate was evaluated under low mechanical loading, appropriate to the strength of the printing resin. Two nickel electrodes of 1 × 1 mm were attached with conductive paste to the two ends of the active zone and connected to a digital multimetre (Agilent 34461A—Keysight Technologies, Santa Rosa, CA, USA). A compressive force was applied periodically with a load cell-based excitation setup at approximately 2.8 Hz (about 0.36 s per cycle in the recorded trace). The test was designed as shown in Figure 3: factors, applied force (levels 1 N and 2 N) and coating (levels uncoated and $BaTiO_3$-coated); responses, the peak-to-peak voltage of each compression–release cycle (V_{pp}) and its standard deviation over the cycles recorded at each level (12 at 1 N and 20 at 2 N), under ambient conditions. Both plates were measured with the same electrodes, wiring, multimetre and excitation, and no poling was applied.

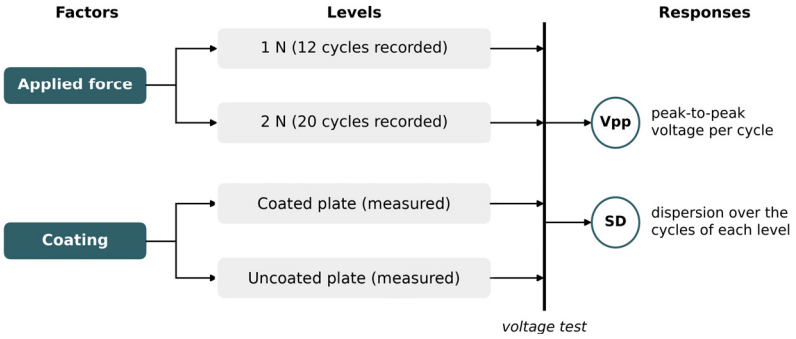


Figure 3. Design of the voltage test: factors, levels and responses. Both coating levels were measured. Layout adapted from Figure 3 of [26].

3. Results

3.1. Dimensional Accuracy and Structural Fidelity of the Printed Scaffold Before Coating

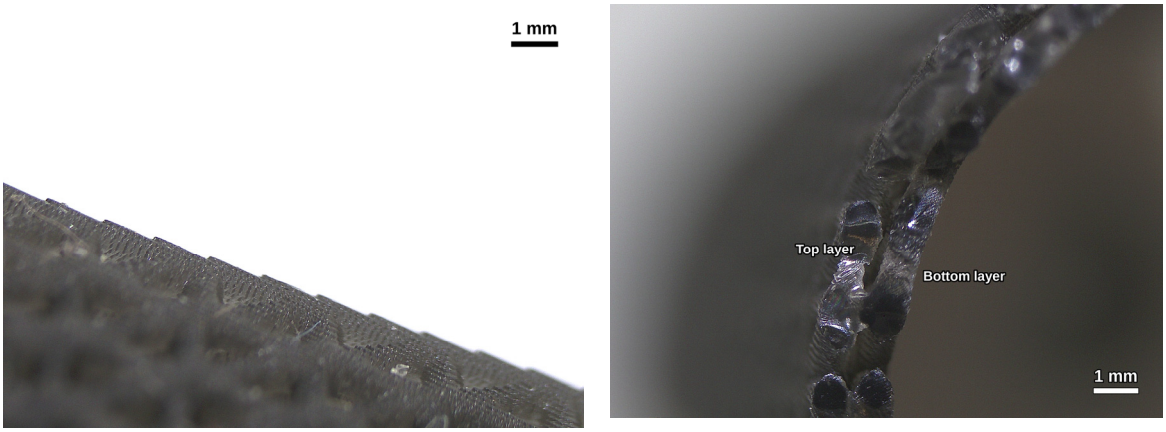
As a preliminary dimensional check on three features (Table 1), the printed plates, measured before coating, gave accuracies of 98.45% (A, +1.55%, oversize), 97.95% (B, −2.05%, undersize) and 99.90% (C, +0.10%, oversize), with an average of 98.77%. The measurements cover three features only; they are not an assessment of the accuracy of the whole porous geometry, for which a surface scan against the CAD model is planned. Resin parts can deviate further at thermal steps after printing: in SLA surgical guides, the scan-to-CAD deviation rose from 0.67 to 0.96 mm after steam sterilisation at 121–134 °C [24]. The coating process exposes the plate to 120 °C drying cycles and a 180 °C solvothermal treatment, and the dimensions were not remeasured afterwards; the values in Table 1 therefore describe the plate as printed, not the final coated prototype, and a post-treatment dimensional check is still required (Section 3.4).

Table 1. CAD versus printed dimensions of the technological zone width (A) and Delaunay unit cell length (B) and height (C). Printed values are single measurements (A) or averages over several unit cells (B, C); the number of measurements and their dispersion were not recorded. Signed deviations are given in the text. All values were measured on the plate as printed, before the coating and thermal treatments.

Dimension [mm]	CAD Model	Print	Accuracy
A—technological zone width	2.586	2.626	98.45%
B—unit cell length	1.319	1.292	97.95%
C—unit cell height	1.012	1.013	99.90%

Optical microscopy of the apex of the plate's curvature (Figure 4a) revealed a stepped, scale-like micro-topology, consistent with the intended breakup of periodicity from the 70%

mesh reduction (Section 2.1), without introducing surface features large enough to further irritate surrounding tissue; these micro-scales may act as anchoring sites for the coating, although its adhesion was not determined (Section 3.4). Cross-sectional imaging showed that the bi-layer scaffold architecture was cleanly reproduced, with no underdeveloped material or pore blockage.



(**a**) (**b**)

Figure 4. (**a**) Scale edge formation on the apex of the dorsal plate (oblique view; the scale bar applies to the plane in focus); (**b**) cross-section of the Delaunay scaffold.

Removal of unreacted liquid resin during post-processing is likely to have contributed to the open bi-layer fidelity. Detached in the green state, the internal channels of the Delaunay lattice are highly susceptible to monomer entrapment [7]. Leveraging the hydrophilic nature of the water-washable resin, agitated water immersion was used to remove excess surface monomer, and high-pressure air jetting to clear residual resin from the orifices, which helps to avoid pore clogging and the artefacts commonly encountered in powder-based fusion (PBF) and similar processes [7,27,28]. Subsequent uniform radiation inside a UV post-curing chamber for ~5 min on a rotating base was intended to complete the polymerisation of residual monomer within the structure and to improve the stability of the polymer during the subsequent thermal cycles [6,29]; the degree of cure and the thermal behaviour of the printed resin were not measured. High-magnification cross-sectional examination showed that the overlapping strut layers remained fully distinct, maintaining open 0.25 mm strut boundaries and unobstructed vertical drainage pathways essential for subsequent liquid coating penetration and tissue vascularisation [8,30].

3.2. Chemical Characterisation of the BTO Coating

Figure 5 compares the Fourier Transform Infrared (FTIR) spectra of a BTO-submerged scaffold and an unsubmerged one; the main bands are listed in Table 2. Both spectra show the aliphatic C–H stretching band of the cured resin near 2900 cm^{-1}. The submerged scaffold additionally shows a broader, higher absorption between about 3600 and 3200 cm^{-1}, attributed to hydrogen-bonded O–H groups (adsorbed water or surface hydroxyls), and two strong bands near 1600 and 1410 cm^{-1}, attributed tentatively to the asymmetric and symmetric stretching of carboxylate (COO^{-}) groups, for example, residual barium propionate from the precursor. A band near 1300 cm^{-1} may arise from carbonate species. Below about 600 cm^{-1}, the absorption of the submerged scaffold rises to a maximum near 500 cm^{-1}, whereas that of the unsubmerged scaffold remains low; this band is assigned tentatively to Ti–O stretching, since Ti–O bands of $BaTiO_3$ are usually reported at about 500–650 cm^{-1} (~650 cm^{-1} in [20]) and amorphous titanates absorb in the same range. The weaker bands marked near 1080 and 810 cm^{-1} were not assigned.

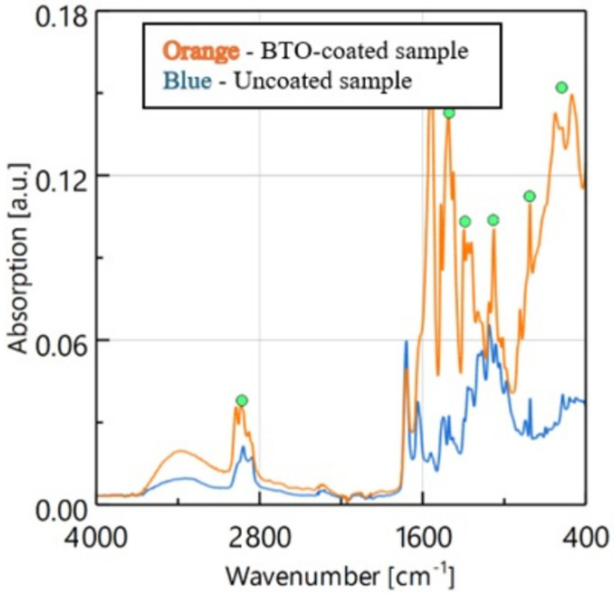


Figure 5. FTIR analysis of the BTO-submerged cured polymeric resin scaffold with an unsubmerged variant. The green markers indicate the bands discussed in the text.

Table 2. Main FTIR bands of the BTO-submerged and unsubmerged scaffolds (Figure 4).

Peak Position [cm^{-1}]	Bond Assignment	Vibration Type	Associated Phase
3600–3200	O–H	H-bonded stretch	Adsorbed water/surface hydroxyls (submerged scaffold)
~2900	C–H	Aliphatic stretch	Cured resin (both scaffolds)
~1600	COO^-	Asymmetric stretch	Carboxylate, e.g., residual propionate (tentative)
~1410	COO^-	Symmetric stretch	Carboxylate (tentative)
~1300	C–O	Asymmetric stretch	Possible carbonate species (tentative)
~500	Ti–O	Lattice stretch	Titanate network (tentative; not specific to crystalline $BaTiO_3$)

To identify the crystalline phase formed after the solvothermal treatment, the coating was analysed by X-ray diffraction (Figure 6). The pattern was recorded on the coated plate in grazing-incidence geometry, at a fixed incidence angle of $\alpha = 0.37°$, which limits the penetration depth of the X-rays to the near-surface region and strongly reduces the contribution of the acrylate resin of the plate, including its amorphous halo between about 15° and 30°. The X-ray diffraction pattern of the coating after the solvothermal treatment (Figure 6) shows well-defined reflections at $2\theta \approx 31.11°$, 37.1°, 43.1°, 57.4° and 66.3°, which are tentatively assigned to the (110), (111), (200), (211) and (220) planes of perovskite $BaTiO_3$ and are indexed according to the $BaTiO_3$ perovskite reference card (JCPDS 05-0626); the tetragonal and cubic polymorphs cannot be distinguished from this pattern alone. No additional reflections that could be attributed to secondary phases, such as $BaCO_3$ or TiO_2, are observed within the sensitivity of the technique. The intense (110) reflection suggests a crystalline phase; crystallite size and strain were not determined.

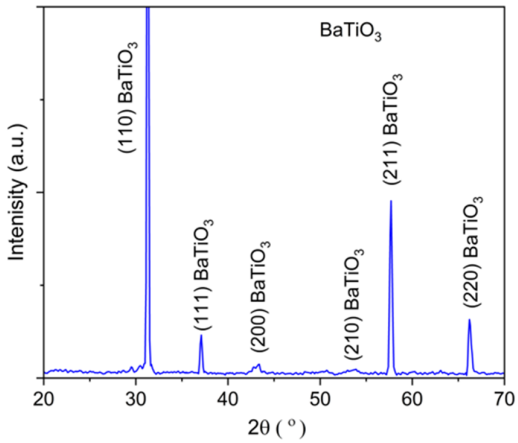
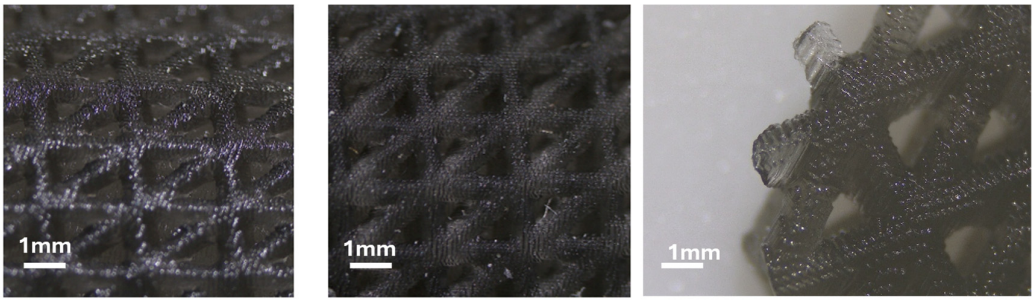


Figure 6. XRD pattern of the barium titanate precursor-derived coating on the printed resin scaffold after solvothermal treatment at 180 °C for 1 h.

To verify the physical presence of the deposited material and assess the morphological changes induced by the coating cycle detailed above, the consolidated sample was brought for microscopic optical imaging (Figure 7). The primary objective of this procedure was to look for surface indicators consistent with a deposited inorganic layer while ensuring that the Delaunay micro-topology remained uncompromised. The coated sample was positioned under a high-resolution Optika microscope (OPTIKA S.r.l., based in Ponteranica (Bergamo), Italy).



(**a**) (**b**) (**c**)

Figure 7. (**a**) Microscopic image of the Delaunay mesh on the BTO-coated resin sample; (**b**) a non-coated sample; (**c**) close-up image of the cross-section of the Delaunay mesh on the BTO-coated resin sample.

Under observation, the captured visual data are consistent with a surface coat. As shown above in Figure 7c, the main visual difference is a bright sheen that reflects across the top edges of the structural struts. While standard, uncoated water-washable resin exhibits a diffuse, flat matte finish, and the BTO-coated sample's surfaces interact with the microscope's light source to produce a highly reflective top layer. This is consistent with an inorganic surface layer formed as the BTO solution was dried during the sequential thermal cycles. The purpose of inspecting the cross-sectional boundaries in a strut is to examine the interface between the core polymeric material and the overlying surface layer. Figure 7c shows that, at this resolution, the 0.25 mm struts and internal cell pathways remain open, with no visible blockages. This supports the previously discussed approach to thermal treatment—cyclic, 15 min thermal consolidation phases—as having produced a coating that follows the contours of the struts, rather than filling in the pores between the micro-geometries, which are required to remain free and unclogged. This observation suggests that the coating procedure preserved the micro-topology of the original design; the thickness and uniformity of the coating were not measured.

SEM images of the coated surface (Figure 8) show a granular, scale-like morphology at the 100 µm scale, without visible cracks or delamination in the imaged area. The EDS maps show barium and titanium distributed over the imaged area, with a few darker regions that correspond to topographic features (pores and shadowed areas) in the micrograph. The maps are qualitative and were recorded on a rough, three-dimensional polymer surface, where shadowing and variations in the take-off angle affect the signal. Because the Ba Lα and Ti Kα lines overlap, the Ba and Ti maps cannot be fully separated, and the maps do not establish the Ba:Ti ratio or the phase. The thickness, adhesion, uniformity and mechanical stability of the coating were not quantified, so these observations indicate qualitative surface coverage only.

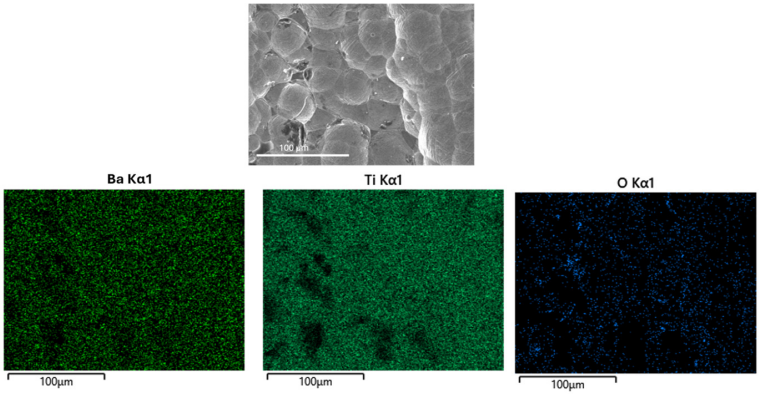


Figure 8. SEM micrograph of the coated surface and corresponding EDS elemental maps of Ba (Lα), Ti (Kα) and O (Kα).

3.3. Illustrative Finite Element Response and Electrical Response

Figure 9 shows the displacement field of the periodic perforated surrogate under the 300 N normal load (nominal MED610 properties, 72.6% porosity). The displacement increases from the fixed technological zones to a maximum of 4.083 mm at the centre of the span. This result is reported only as an illustrative response of the surrogate model. The study was not run on the Delaunay lattice, did not use the properties of the printed resin, and did not include mesh convergence, stress evaluation, buckling, large-displacement effects or experimental validation (Section 2.4); it therefore provides no evidence of the mechanical suitability of the plate, which requires mechanical testing of the printed structure (Section 3.4).

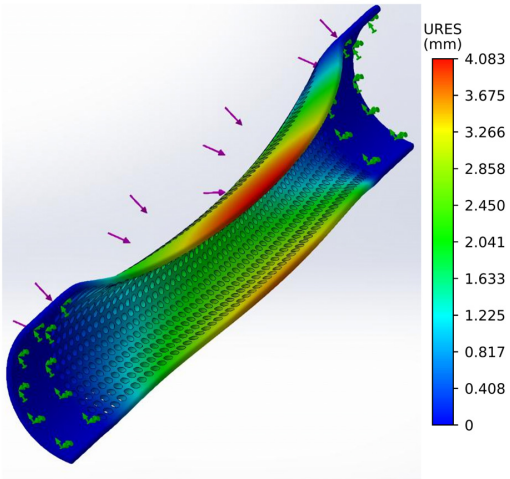


Figure 9. Displacement (URES) of the periodic perforated surrogate under the 300 N normal load (linear static study, nominal MED610 properties).

To establish a baseline, the same test was first applied to an uncoated plate printed in the same resin, with the same electrodes, wiring and multimetre, at the same force levels (Figure 10a). The uncoated plate gave an alternating signal of low amplitude at both 1 N and 2 N, well below 0.1 V on the scale of the figure. Under the same loading, the $BaTiO_3$-coated plate prototype gave much larger and clearly distinguishable open-circuit voltage responses at the two force levels (Figure 10b). At ~1 N (12 cycles, approximately 0–4 s of the recorded trace), the peak-to-peak voltage was 0.62 ± 0.08 V (mean ± SD), with positive peaks of about 0.25–0.45 V; when the applied force was increased to ~2 N (20 cycles, approximately 7–15 s), it rose to 0.93 ± 0.10 V, with positive peaks of about 0.3–0.6 V.

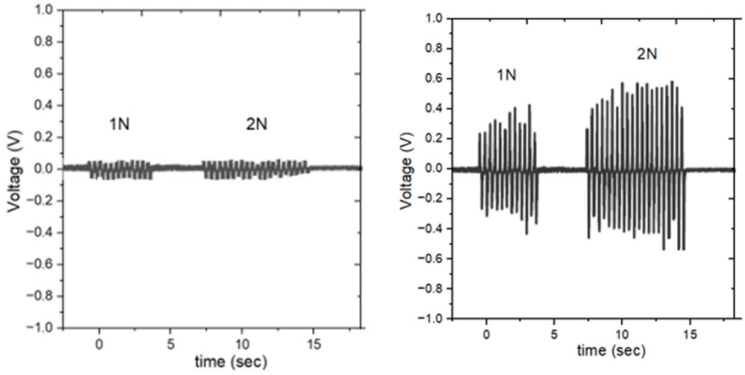


Figure 10. Time-dependent open-circuit voltage under periodic mechanical excitation at 1 N and 2 N: (**a**) uncoated plate; (**b**) $BaTiO_3$-coated plate. Both panels have the same voltage scale and the same force levels.

The signal was alternating, with a positive and a negative peak in each compression–release cycle, and its amplitude was higher at 2 N than at 1 N on the tested sample. These data show a force-dependent electromechanical voltage response that is much larger with the coating than without it, so the response depends on the coated surface. They do not by themselves establish that it originates from a piezoelectric $BaTiO_3$ layer, because the coating may also change the triboelectric and electrostatic behaviour of the surface, the $BaTiO_3$ polymorph was not resolved, and no poling was applied. The recorded peak-to-peak amplitude (0.62–0.93 V) is also much larger than that measured on crystalline $BaTiO_3$ films obtained by the same chemical route [20] (about 10–18 mV), although the substrates, electrodes and measurement geometries differ, which reinforces the need for poled and replicate measurements before any piezoelectric attribution. The waveform was stable and repeatable over the recorded cycles. The dependence of the amplitude on force is based on two force levels measured on a single sample of each type and should be confirmed with replicate samples and additional force levels.

3.4. Limitations

This is a proof-of-concept study with several limitations. (i) The printing resin is not biocompatible, and the mechanical properties of the printed plate were not measured; the finite element study used nominal MED610 properties on a periodic surrogate. (ii) Dimensional accuracy was assessed on three features of the plate as printed and was not remeasured after the thermal steps (120 °C drying and 180 °C solvothermal), which can deform thin resin parts [24]; the reported accuracy therefore does not describe the final coated prototype. (iii) Because the coating is the main functional element of the prototype, its incomplete characterisation is a central limitation: the polymorph, thickness, adhesion, uniformity and mechanical stability of the coating were not quantified, and EDS is qualitative. The coating results are therefore limited to qualitative surface coverage

and phase-consistent XRD evidence. (iv) The voltage response was obtained on a single sample that had not undergone the solvothermal treatment, at two force levels, without poling or replicates, and was compared with a single uncoated plate, so its piezoelectric origin is not established. (v) No biological testing was performed (no cytotoxicity, cell response, osteogenic evaluation, coating stability in physiological media, degradation or leaching analysis, sterilisation study or biocompatibility testing after coating). (vi) No mesh convergence study, failure analysis, safety factor, fatigue test, screw-hole assessment or multiaxial loading was performed, and Raman spectroscopy was not used to confirm the phase. These points define the next steps: mechanical testing of printed lattices, fabrication in a biocompatible resin, quantitative coating characterisation, controlled piezoelectric measurements and biological evaluation.

4. Conclusions

(i) Design and printing. A curved, 0.5 mm $BaTiO_3$-coated dorsal fixation plate prototype with a randomised, 70%-reduced Delaunay lattice was designed and printed by consumer-grade masked stereolithography. The CAD active zone has a porosity of 73.6%. Three features of the printed plates, measured before coating, were reproduced with an average accuracy of 98.77% (the dimensions after the 120 °C and 180 °C steps were not measured), and the 0.25 mm strut pathways remained open. A linear static finite element study of a periodic surrogate is reported only as an illustrative response (peak displacement 4.083 mm at 300 N) and does not establish the mechanical suitability of the plate. (ii) Coating and electrical response. A barium titanate coating applied by three low-temperature submersion cycles and a solvothermal treatment at 180 °C was examined by XRD and SEM/EDS after the solvothermal treatment, and by FTIR and optical microscopy on plates dried at 120 °C only, before the solvothermal step was introduced. The results are limited to qualitative surface coverage with open pores and XRD reflections consistent with perovskite $BaTiO_3$; the polymorph, thickness, adhesion, uniformity and mechanical stability of the coating were not quantified. A coated plate dried at 120 °C only gave a repeatable, force-dependent open-circuit voltage (peak-to-peak 0.62 ± 0.08 V at 1 N and 0.93 ± 0.10 V at 2 N), much larger than that of an uncoated plate, but without poling or replicate measurements, its piezoelectric origin is not established. (iii) Limitations and next steps. The work is therefore a fabrication and preliminary characterisation study of a non-biocompatible prototype that has not undergone mechanical validation, confirmed piezoelectric characterisation or biological testing. The next steps are mechanical testing of printed lattices, fabrication in a biocompatible resin, quantitative coating characterisation, controlled piezoelectric measurements on replicate and poled samples, and biological evaluation.

Author Contributions: Conceptualisation, E.G.T. and M.N.; methodology, E.G.T. and M.N.; software, E.G.T.; validation, E.G.T., M.N. and R.P.; formal analysis, E.G.T. and M.N.; investigation, E.G.T. and M.N.; resources, E.G.T. and M.N.; data curation, E.G.T. and M.N.; writing—original draft preparation, E.G.T.; writing—review and editing, E.G.T. and M.N.; visualisation, E.G.T. and M.N.; supervision, R.P.; project administration, R.P.; funding acquisition, R.P. All authors have read and agreed to the published version of the manuscript.

Funding: This research was supported by the ERASMUS+ Partnerships for cooperation and exchanges of practices (KA220)—"Biomedical Innovations through Digital Transformation of Additive Technologies and Knowledge Exchange—BIOMEDIX"—Project No. 2024-1-LV01-KA220-HED-000255929.

Data Availability Statement: The original contributions presented in this study are included in the article. Further inquiries can be directed to the corresponding author.

Conflicts of Interest: The authors declare no conflicts of interest.

Abbreviations

The following abbreviations are used in this manuscript:

BTO	Barium Titanate
CCS	Cannulated Compression Screw
FEA	Finite Element Analysis
3D	Three-Dimensional
CAD	Computer-Aided Design
FTIR	Fourier Transform Infrared
MSLA	Masked Stereolithography
XRD	X-ray Diffraction
SEM	Scanning Electron Microscopy
EDS	Energy-Dispersive X-ray Spectroscopy

References

1. Nemirov, D.; Kasper, A.A.; Sherman, M.; Siddiqui, H.; Ilyas, A.M.; Hozack, B. Metacarpal Fracture Trends in Treatment: A Matched Cohort Analysis of 1022 Patients. *Arch. Bone Jt. Surg.* **2025**, *13*, 489–496.
2. Deuschl, J.; Alfort, H.; Wilcke, M. The Epidemiology of Metacarpal Fractures: A Descriptive Study Based on 18,802 Fractures from the Swedish Fracture Register. *J. Hand Surg. Glob. Online* **2025**, *7*, 100725. [CrossRef]
3. Sohn, R.C.; Jahng, K.H.; Curtiss, S.B.; Szabo, R.M. Comparison of Metacarpal Plating Methods. *J. Hand Surg.* **2008**, *33*, 316–321. [CrossRef]
4. Matzon, J.L.; Kenniston, J.; Beredjiklian, P.K. Hardware-Related Complications After Dorsal Plating for Displaced Distal Radius Fractures. *Orthopedics* **2014**, *37*, 11. [CrossRef]
5. Nicoletti, D.; Knipe, H. Stress Shielding After Fracture Fixation. Radiopaedia.org. 2023. Available online: https://radiopaedia.org/articles/stress-shielding-after-fracture-fixation?lang=us (accessed on 25 June 2026).
6. Bukhari, S.M.Z.S.; Bukhari, M.A.; Hossain, M. Vat Photopolymerization of Smart Polymers for Biomedical Applications. *ACS Appl. Polym. Mater.* **2025**, *7*, 12117–12144. [CrossRef]
7. Stratasys. Design for Additive Manufacturing with PolyJet. Available online: https://d2pye4zfc3qqup.cloudfront.net/wp-content/uploads/2020/08/18145504/Best-Practice-Design-for-Additive-Manufacturing-with-PolyJet.pdf (accessed on 25 June 2026).
8. Zenobi, E.; Merco, M.; Mochi, F.; Ruspi, J.; Pecci, R.; Marchese, R.; Convertino, A.; Lisi, A.; Del Gaudio, C.; Ledda, M. Tailoring the Microarchitectures of 3D Printed Bone-like Scaffolds for Tissue Engineering Applications. *Bioengineering* **2023**, *10*, 567. [CrossRef]
9. Kanwar, S.; Al-Ketan, O.; Vijayavenkataraman, S. A novel method to design biomimetic, 3D printable stochastic scaffolds with controlled porosity for bone tissue engineering. *Mater. Des.* **2022**, *220*, 110857. [CrossRef]
10. Mueller, J.; Matlack, K.H.; Shea, K.; Daraio, C. Energy Absorption Properties of Periodic and Stochastic 3D Lattice Materials. *Adv. Theory Simul.* **2019**, *2*, 1900081. [CrossRef]
11. Yamada, S.; Suzuki, H.; Sawada, K.; Okada, S.; Nishimura, A.; Todoh, M. Novel strut-based stochastic lattice biomimetically designed based on the structural and mechanical characteristics of cancellous bone. *Mater. Des.* **2025**, *251*, 113657. [CrossRef]
12. Zhou, Z.; Qian, D.; Minary-Jolandan, M. Molecular Mechanism of Polarization and Piezoelectric Effect in Super-Twisted Collagen. *ACS Biomater. Sci. Eng.* **2016**, *2*, 929–936. [CrossRef]
13. Jacob, J.; More, N.; Kalia, K.; Kapusetti, G. Piezoelectric smart biomaterials for bone and cartilage tissue engineering. *Inflamm. Regen.* **2018**, *38*, 2. [CrossRef]
14. Ganeson, K.; May, C.T.X.; Abdullah, A.A.A.; Ramakrishna, S.; Vigneswari, S. Advantages and Prospective Implications of Smart Materials in Tissue Engineering: Piezoelectric, Shape Memory, and Hydrogels. *Pharmaceutics* **2023**, *15*, 2356. [CrossRef]
15. Zhang, J.; Liu, C.; Li, J.; Yu, T.; Ruan, J.; Yang, F. Advanced Piezoelectric Materials, Devices, and Systems for Orthopedic Medicine. *Adv. Sci.* **2025**, *12*, 2410400. [CrossRef]
16. Carter, A.; Popowski, K.; Cheng, K.; Greenbaum, A.; Ligler, F.S.; Moatti, A. Enhancement of Bone Regeneration Through the Converse Piezoelectric Effect, A Novel Approach for Applying Mechanical Stimulation. *Bioelectricity* **2021**, *3*, 255–271. [CrossRef]
17. Zheng, Y.; Zhao, L.; Li, Y.; Zhang, X.; Zhang, W.; Wang, J.; Liu, L.; An, W.; Jiao, H.; Ma, C. Nanostructure Mediated Piezoelectric Effect of Tetragonal $BaTiO_3$ Coatings on Bone Mesenchymal Stem Cell Shape and Osteogenic Differentiation. *Int. J. Mol. Sci.* **2023**, *24*, 4051. [CrossRef]
18. Sahoo, R.; Sanket, A.S.; Pattnaik, A.; Pany, S.; Pradhan, S.; Pati, S.; Haugen, H.J.; Puppi, D.; Samal, S.K. Designing of porous scaffolds for tissue engineering and regenerative medicine. *J. Mater. Chem. B* **2026**, *14*, 2733–2773. [CrossRef]

19. Shyeed, M.A.; Ferdaus, J.; Hossain, M.F.; Hossain, M.A.; Hossain, K.R. Polymer-Based Smart Material in 4D Printing Applications. *Smart Wearable Technol.* **2025**, *2*, A2. [CrossRef]
20. Nasui, M.; Sonher, R.; Petrisor, T.; Ware, E.; Tuns, E.; Pacurar, R.; Gabor, M. New approach for oriented $BaTiO_3$ thin films with piezoelectric properties through chemical synthesis. *J. Alloys Compd.* **2025**, *1036*, 182008. [CrossRef]
21. AO Foundation. Headless Compression Screw Insertion. AO Surgery Reference: Adult Trauma, Basic Technique. Available online: https://surgeryreference.aofoundation.org/orthopedic-trauma/adult-trauma/basic-technique/headless-compression-screw (accessed on 9 June 2026).
22. Murawski, C.D.; Reddy, R.P.; Tisherman, R.T.; Bosch, P.P.; Grudziak, J.S.; Mendelson, S.A.; Ward, W.T.; Olgun, Z.D. Thread Delamination in 4.5 mm AO Cannulated Screws: A Small Case Series in the Pediatric Trauma Population. *J. Pediatr. Orthop.* **2022**, *42*, e257–e261. [CrossRef]
23. Neto, F.N.D.M.; Fialho, A.C.V.; de Moura, W.L.; Rosa, A.G.F.; de Matos, J.M.E.; Reis, F.d.S.; Mendes, M.T.D.A.; Sales, E.S.D. Castor polyurethane used as osteosynthesis plates: Microstructural and thermal analysis. *Polímeros* **2019**, *29*, e2019029. [CrossRef]
24. Salerno, F.; Moos, S.; Ulrich, L.; Novaresio, A.; Vezzetti, E. A Methodology for the Dimensional and Mechanical Analysis of Surgical Guides. In *Design Tools and Methods in Industrial Engineering III (ADM 2023)*; Carfagni, M., Furferi, R., Di Stefano, P., Governi, L., Gherardini, F., Eds.; Lecture Notes in Mechanical Engineering; Springer: Cham, Switzerland, 2024; pp. 184–193. [CrossRef]
25. Tilton, M.; Lewis, G.S.; Wee, H.B.; Armstrong, A.; Hast, M.W.; Manogharan, G. Additive manufacturing of fracture fixation implants: Design, material characterization, biomechanical modeling and experimentation. *Addit. Manuf.* **2020**, *33*, 101137. [CrossRef]
26. Salerno, F.; Ulrich, L.; Maculotti, G.; Moos, S.; Genta, G.; Vezzetti, E.; Galetto, M. A metrological approach for Augmented Reality tooltip tracking assessment. *Comput. Ind.* **2026**, *175*, 104430. [CrossRef]
27. Rott, S.; Ladewig, A.; Friedberger, K.; Casper, J.; Full, M.; Schleifenbaum, J.H. Surface roughness in laser powder bed fusion—Interdependency of surface orientation and laser incidence. *Addit. Manuf.* **2020**, *36*, 101437. [CrossRef]
28. Islam, A.; Rahman, M.Z. Recent advances in additive manufacturing techniques: An in-depth review. In *Comprehensive Materials Processing*; Elsevier: Amsterdam, The Netherlands, 2024; pp. 352–378. [CrossRef]
29. Dizon, J.R.C.; Espera, A.H.; Chen, Q.; Advincula, R.C. Mechanical characterization of 3D-printed polymers. *Addit. Manuf.* **2018**, *20*, 44–67. [CrossRef]
30. Wang, C.; Huang, W.; Zhou, Y.; He, L.; He, Z.; Chen, Z.; He, X.; Tian, S.; Liao, J.; Lu, B.; et al. 3D printing of bone tissue engineering scaffolds. *Bioact. Mater.* **2020**, *5*, 82–91. [CrossRef]

Disclaimer/Publisher's Note: The statements, opinions and data contained in all publications are solely those of the individual author(s) and contributor(s) and not of MDPI and/or the editor(s). MDPI and/or the editor(s) disclaim responsibility for any injury to people or property resulting from any ideas, methods, instructions or products referred to in the content.